Metal (Ni, Co)-Metal Oxides/Graphene Nanocomposites as Multifunctional Electrocatalysts

Xien Liu, Wen Liu, Minseong Ko, Minjoon Park, Min Gyu Kim, Pilgun Oh, Sujong Chae, Suhyeon Park, Anix Casimir, Gang Wu, and Jaephil Cho**

Oxygen reduction reaction (ORR) and oxygen evolution reaction (OER) along with hydrogen evolution reaction (HER) have been considered critical processes for electrochemical energy conversion and storage through metal-air battery, fuel cell, and water electrolyzer technologies. Here, a new class of multifunctional electrocatalysts consisting of dominant metallic Ni or Co with small fraction of their oxides anchored onto nitrogen-doped reduced graphene oxide (rGO) including Co-CoO/N-rGO and Ni-NiO/N-rGO are prepared via a pyrolysis of graphene oxide and cobalt or nickel salts. Ni-NiO/N-rGO shows the higher electrocatalytic activity for the OER in 0.1 M KOH with a low overpotential of 0.24 V at a current density of 10 mA cm^{-2}, which is superior to that of the commercial IrO_2. In addition, it exhibits remarkable activity for the HER, demonstrating a low overpotential of 0.16 V at a current density of 20 mA cm^{-2} in 1.0 M KOH. Apart from similar HER activity to the Ni-based catalyst, Co-CoO/N-rGO displays the higher activity for the ORR, comparable to Pt/C in zinc-air batteries. This work provides a new avenue for the development of multifunctional electrocatalysts with optimal catalytic activity by varying transition metals (Ni or Co) for these highly demanded electrochemical energy technologies.

1. Introduction

Development of clean electrochemical energy conversion and storage technologies such as fuel cells, metal-air batteries, and water electrolyzers is highly desirable to address current issues associated with energy security and environmental pollution.[1–5] Oxygen reduction reaction (ORR), oxygen evolution reaction (OER), and hydrogen evolution reaction (HER) are the most crucial electrochemical reactions to realize energy storage and conversion in these technologies. Although Pt-, Ir-, and Ru-based materials exhibit the highest activity for these electrochemical reactions, these precious-metal catalysts cannot be largely used for these clean energy because of their scarcity on earth and high cost.[6,7] Therefore, high-active, low-cost, and durable precious-metal-free catalysts from earth-abundant elements have been attracted considerable attention since last decade.[8–11] Among studied nonprecious metal catalysts,[12] nickel and cobalt are earth-abundant, low-cost, and environment-friendly materials that have widely been explored as electrocatalysts for the oxygen or hydrogen reactions in energy conversion and storage devices.[13–15] However, the pure cobalt and nickel oxides usually show insufficient electrical conductivity and low reactive surface areas, resulting in limited kinetics during these electrochemical reactions such as ORR, OER.[16] Oppositely, standalone metallic Ni or Co has good electrical conductivity, but is less active than Pt, because the formation energies of Ni–H or Co–H is lower than that of Pt–H for the HER.[17] Furthermore, combining graphene with metal or metal oxide is an effective way to improve catalytic activities due to the high surface area and excellent electrical conductivity of graphene,[18–20] thereby increasing number of active sites and promoting the charge transfer in electrodes.[21–23] For example, Co_3O_4/graphene,[24] Ni/graphene film,[25] and NiO/rGO[26] composite catalysts have been explored showing enhanced catalytic activity, relative to single metals or metal oxides. Based on previous studies on the nickel or cobalt electrocatalysts, in this work, we synthesized a new family catalyst including Co-CoO/N-rGO and Ni-NiO/N-rGO via a pyrolysis of graphene oxide-supported cobalt and nickel salts, respectively. The possible synergetic effect among transition metals, metal oxides, and graphene was systematically studied, making them simultaneously highly active for the OER, ORR, or HER.

Dr. X. Liu, W. Liu, M. Ko, M. Park, P. Oh, S. Chae, S. Park, Prof. J. Cho
Department of Energy Engineering
School of Energy and Chemical Engineering
Ulsan National Institute of Science and Technology (UNIST)
Ulsan 689-798, South Korea
E-mail: jpcho@unist.ac.kr
Dr. M. G. Kim
Beamline Research Division
Pohang Accelerator Laboratory (PAL)
Pohang 790-784, South Korea
A. Casimir, Prof. G. Wu
Department of Chemical and Biological Engineering
University at Buffalo, State University of New York
Buffalo, NY 14260, USA
E-mail: gangwu@buffalo.edu

DOI: 10.1002/adfm.201502217

2. Results and Discussion

In order to provide comprehensive structural information, the synthesized Co-CoO/N-rGO and Ni-NiO/N-rGO catalysts were extensively characterized by using scanning electron microscopy (SEM), high-resolution transmission electron microscopy (HRTEM), X-ray diffraction (XRD), X-ray photoelectron spectroscopy (XPS), X-ray absorption near-edge structure (XANES), and extended X-ray absorption fine structure (EXAFS) spectroscopy. During the catalyst preparation, we also studied the structural changes of precursors under different conditions. The SEM image shows that the $Co(CO_3)_{0.5}(OH)\cdot 0.11H_2O$ precursor wrapped with rGO (Figure S1a, Supporting Information) yields a loose and porous morphology of CoO/N-rGO after a high-temperature treatment (Figure S1b, Supporting Information). Figure S1c,d (Supporting Information) shows low magnitude SEM and transmission electron microscopy (TEM) images. The rGO remains well-dispersed morphology even after the annealing procedure. The SEM image of Co-CoO/N-rGO shows that the twisted and compacted nanorods with submicrometer lengths were dominated and wrapped with N-rGO (**Figure 1**a). The XRD patterns of Co-CoO/N-rGO and Ni-NiO/N-rGO indicate the peaks at 44.3°, 51.5°, and 75.9° belong to (111), (200), and (220) crystal planes, respectively, for a fcc-structured metallic Co or Ni (JCPDS 15-0806 and 04-0850) (Figure 1b).[27,28] Furthermore, HRTEM images (Figure 1) of Co-CoO/N-rGO identified *d*-spacing values of 2.12 and 2.06 Å, corresponding to the (200) crystal planes for CoO and (111) for Co, respectively. In addition, high-angle annular dark field scanning transmission electron microscopy energy-dispersive

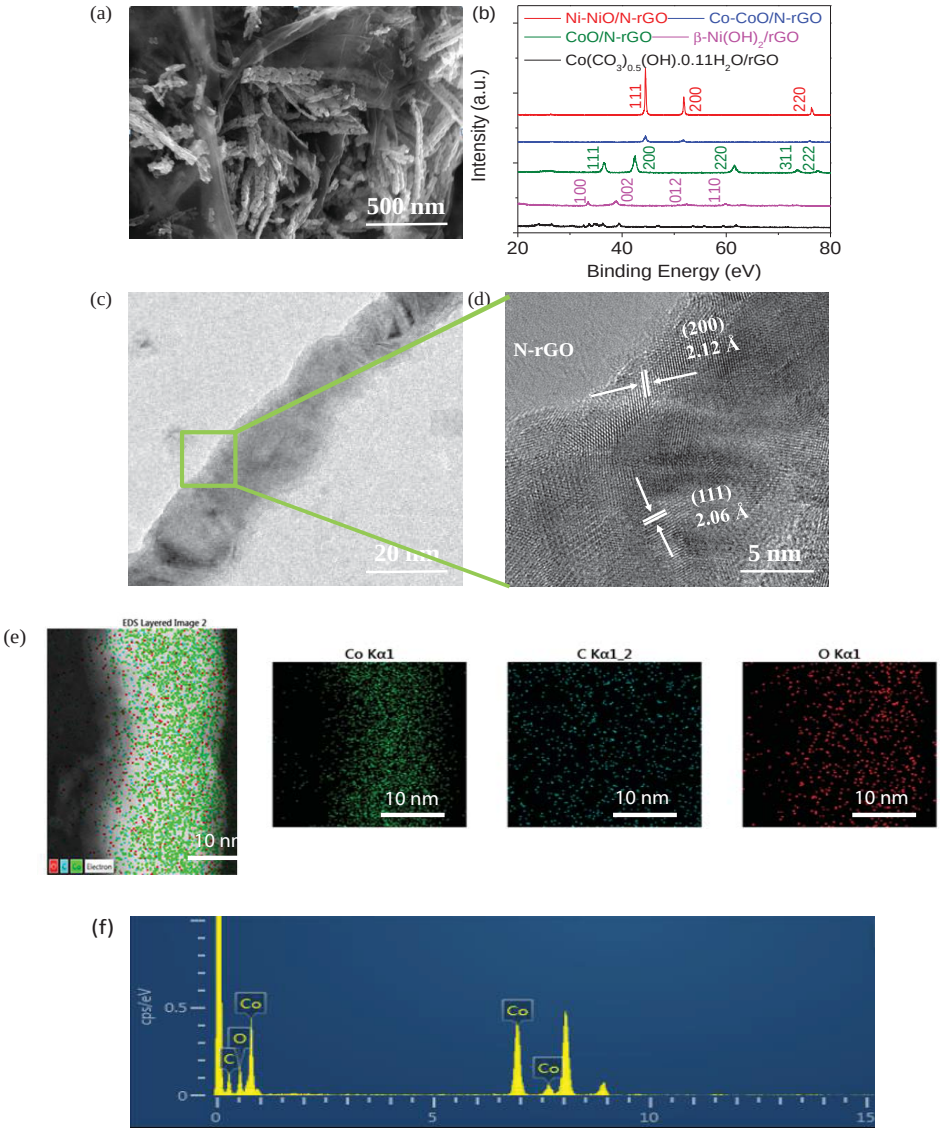

Figure 1. a) SEM image of Co-CoO/N-rGO. b) XRD spectra of the Co-CoO/N-rGO, Ni-NiO/N-rGO, CoO/N-rGO, $Co(CO_3)_{0.5}(OH)\cdot 0.11H_2O$/rGO, and β-$Ni(OH)_2$/rGO. c) Low-magnification and d) high-magnification TEM images of CoO/Co-N-rGO-L. e,f) HAADF-STEM-EDS images of Co-CoO/N-rGO.

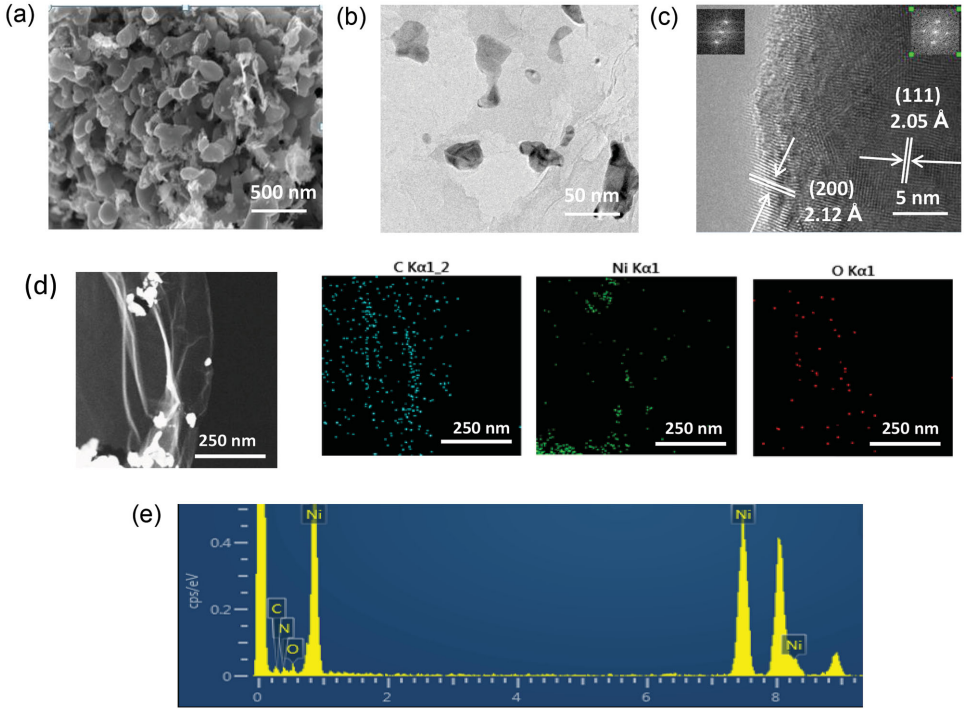

Figure 2. a) The SEM image of Ni-NiO/N-rGO. b,c) TEM images of Ni-NiO/N-rGO. d,e) HAADF-STEM-EDS images of Ni-NiO/N-rGO.

spectroscopy (HAADF-STEM-EDS) mapping was used to examine the elemental distribution in the Co-CoO/N-rGO. All elements including C, Co, and O are shown in Figure 1e,f except for elemental N due to its low content. The carbon distribution of Figure 1e was from graphene layer, instead of lacey carbon film of TEM grids, which can be clearly observed from the TEM image (see Figure S2, Supporting Information). Meanwhile, the SEM and TEM images of Ni-NiO/N-rGO were also shown in **Figure 2**a–e. The SEM image reveals a formation of nanoparticles with the average sizes of 100–150 nm (Figure 2a). HRTEM clearly verifies the formation of catalyst nanoparticles onto graphene sheets (Figure 2b,c). The lattice fringes with widths of 2.12 and 2.05 Å are assigned to (200) and (111) crystal planes of fcc structures of NiO and Ni, respectively (Figure 2c). HAADF and STEM coupled with EDS mapping were used to examine elemental distribution in the Ni-NiO/N-rGO (Figure 2d,e). The analysis of HRTEM combined with STEM-EDS indicates that Ni-NiO/N-rGO is composed of dominant metallic Ni with minor oxides composited with the N-rGO. Based on these SEM images (Figures 1a and 2a), Co-CoO/N-rGO nanorods and Ni-NiO/N-rGO nanoparticles were directly anchored on reduced N-doped graphene oxide sheets, providing enhanced electrical and chemical coupling between the metals/oxides and N-rGO. The intimate bonding and synergetic coupling arisen from active nanocrystals and N-rGO were proved to be favorable to improving electrocatalytic activity for the ORR.[24] In turn, large-surface area rGO is able to well-disperse metal or oxide particles and prevent their possible aggregation, thereby increasing number of active sites.

The surface compositions of both catalysts are further examined by XPS, XANES, and EXAFS, which provides insightful chemical and structural information. At first, high resolution XPS of Co2p for Co-CoO/N-rGO exhibits a low-energy band ($Co2p_{3/2}$) and a high-energy band ($Co2p_{1/2}$) at 781.0 and 796.7 eV with two satellites at 786 and 802 eV, respectively, which both belong to Co^{2+} (**Figure 3**a).[29] In addition, a shoulder at 778.5 eV in Co-CoO/N-rGO suggests the presence of metallic Co in the surface layers.[30] The Ni^{2+} also was clearly identified by the $Ni2p_{3/2}$ (855.7 eV) and $Ni2p_{1/2}$ (873.1 eV) peaks for Ni2p of Ni-NiO/N-rGO with two satellites at 861.3 and 879.9 eV (Figure 3b). The shoulder at 852.8 eV in Ni-NiO/N-rGO also indicates the presence of metallic Ni.[31] The full XPS spectra of Co-CoO/N-rGO and Ni-NiO/N-rGO are compared in Figure S3a,b (Supporting Information). High resolution XPS of O1s of Co-CoO/N-rGO and Ni-NiO/N-rGO also indicate the formation Co–O and Ni–O bond evidenced by the peaks at 529.9 eV (Figure S3c,d, Supporting Information). The XANES for Co K-edge of $Co(CO_3)_{0.5}(OH)\cdot 0.11H_2O$/rGO, CoO/N-rGO, and Co-CoO/N-rGO are shown in Figure 3c. The peak at 7726 eV in the spectrum of CoO/N-rGO is typically assigned to the transition of Co^{2+} from Co 1s to Co 4p mixed state with O 2p. The local environment of Co at CoO/N-rGO was very similar to that in CoO.[32] In good agreement with XPS analysis, the shoulder at 7712 eV in the spectrum of Co-CoO/N-rGO indicates the presence of metallic Co species. Notable, the EXAFS for CoO/N-rGO is very different to those of Co-CoO/N-rGO (Figure 3d). The peak at 1.68 Å for CoO/N-rGO corresponds to Co–O interactions; the peaks at ≈2.6 Å correspond to Co–Co interactions. However, the strongest peaks at 2.2 Å for Co-CoO/N-rGO is attributed to Co–Co interactions from major metallic Co part, and the weak shoulder at ≈2.8 Å is assigned to Co–Co interactions from minor CoO part. Other peaks of Co-CoO/N-rGO at ≈3.3, 4.0, and 4.6 Å are also similar to those of Co foils. Figure 3e shows the XANES of Ni K-edge in

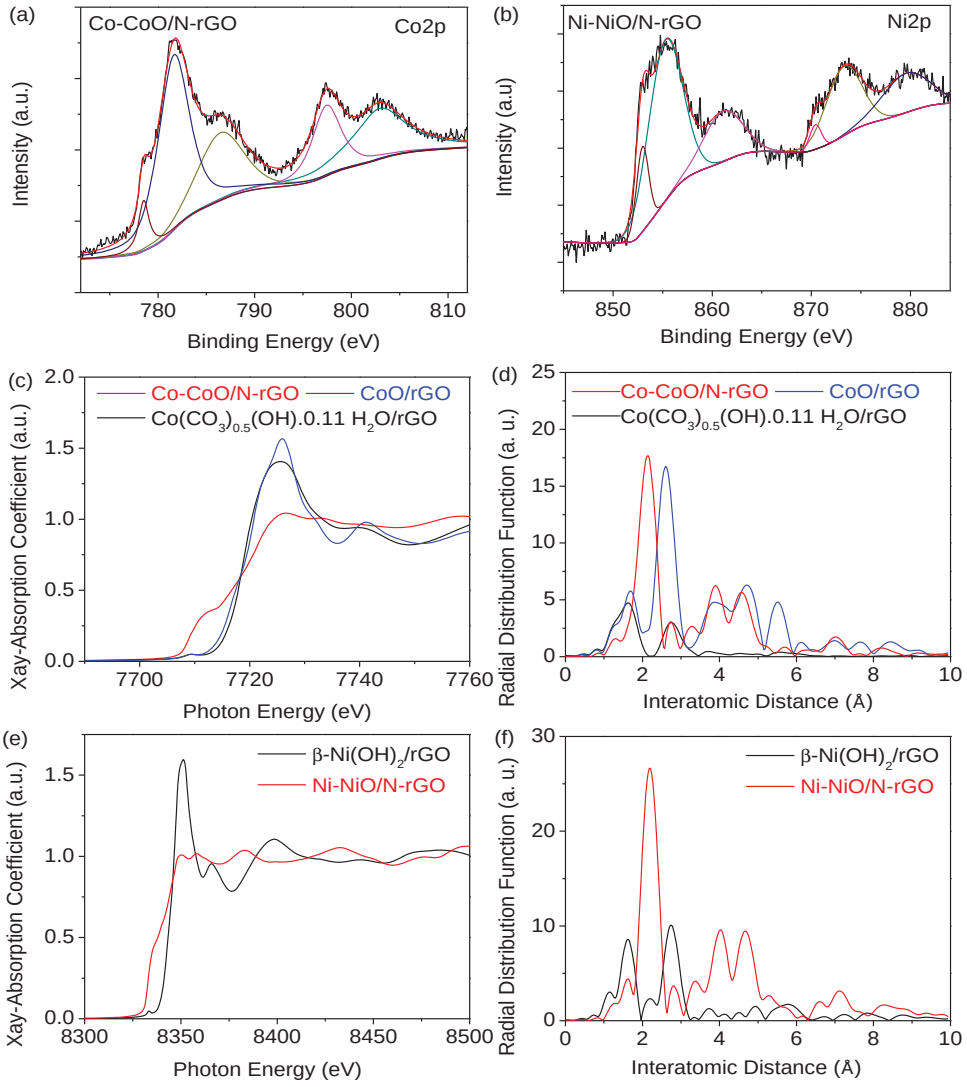

Figure 3. a) XPS spectra of Co2p for Co-CoO/N-rGO in the range of 770–810 eV. b) XPS spectra of Ni2p for Ni-NiO/N-rGO in the range of 844–884 eV. c) XANES spectra for Co K-edge of $Co(CO_3)_{0.5}(OH)\cdot 0.11H_2O$/rGO, CoO/N-rGO, and Co-CoO/N-rGO. d) EXAFS spectra for Co K-edge of $Co(CO_3)_{0.5}(OH)\cdot 0.11H_2O$/rGO, CoO/N-rGO and Co-CoO/N-rGO. e) XANES spectra for Ni K-edge of β-$Ni(OH)_2$/rGO and Ni-NiO/N-rGO. f) EXAFS spectra for Ni K-edge of β-$Ni(OH)_2$/rGO and Ni-NiO/N-rGO.

β-$Ni(OH)_2$/rGO and Ni-NiO/N-rGO. The peaks at 8351, 8365, and 8398 eV in β-$Ni(OH)_2$/rGO were consistent with those of reported β-$Ni(OH)_2$.[33] The shoulder at 8336 eV in Ni-NiO/N-rGO indicates the presence of metallic Ni species. Meanwhile, the EXAFS for β-$Ni(OH)_2$/rGO is also very different to those of Ni-NiO/N-rGO (Figure 3f). The peak at 1.6 Å for β-$Ni(OH)_2$/rGO corresponds to Ni–O interactions, and the peaks at 2.7 and 5.8 Å correspond to Ni–Ni interactions. The strongest peak at 2.2 Å for N-rGO/NiO-Ni is attributed to Ni–Ni interactions from major metallic Ni part, and the weak shoulder at 2.8 Å is assigned to Ni–Ni interactions from minor NiO part. Other peaks of Ni-NiO/N-rGO at 3.3, 4.0, and 4.7 Å are also similar to those of Ni foils, associated with metallic Ni species.[34] A composite consisting of metallic species and their oxides is favorable to enhance electrochemical redox reaction reactivity in the system because of the coexisting various valence state of Ni^0 (Co^0) and Ni^{2+} (Co^{2+}). Such a kind of composite is able to yield high activity for multifunctional electrocatalysis. For example, Ni^0 (Co^0) is mainly contributed to HER, while Ni^{2+} (Co^{2+}) is beneficial to ORR or OER. Importantly, these composites containing Ni^0 (Co^0), Ni^{2+} (Co^{2+}), and N-doped graphene would yield a synergetic role to simultaneously promote the electrocatalytic activities for the HER, ORR, or OER.

Figure 4a shows the OER linear-sweep voltammetry for Ni-NiO/N-rGO, Co-CoO/N-rGO, and bench-mark IrO_2 in 0.1 M KOH electrolyte. When catalyst loading is 0.21 mg cm^{-2} for the half-cell tests, a current density of 10 mA cm^{-2} only generated an overpotential of 0.24 V on the Ni-NiO/N-rGO catalyst, which is much smaller than overpotentials measured with IrO_2 (0.33 V) and Co-CoO/N-rGO (0.39 V). Thus, the Ni-NiO/N-rGO significantly outperforms the IrO_2 and Co-CoO/N-rGO for the OER. In Figure 4b, the Tafel slopes were calculated to be 43, 68, and 56 mV dec^{-1} for these catalysts, respectively. Lower Tafel slope calculated for Ni-NiO/N-rGO suggested a more favorable

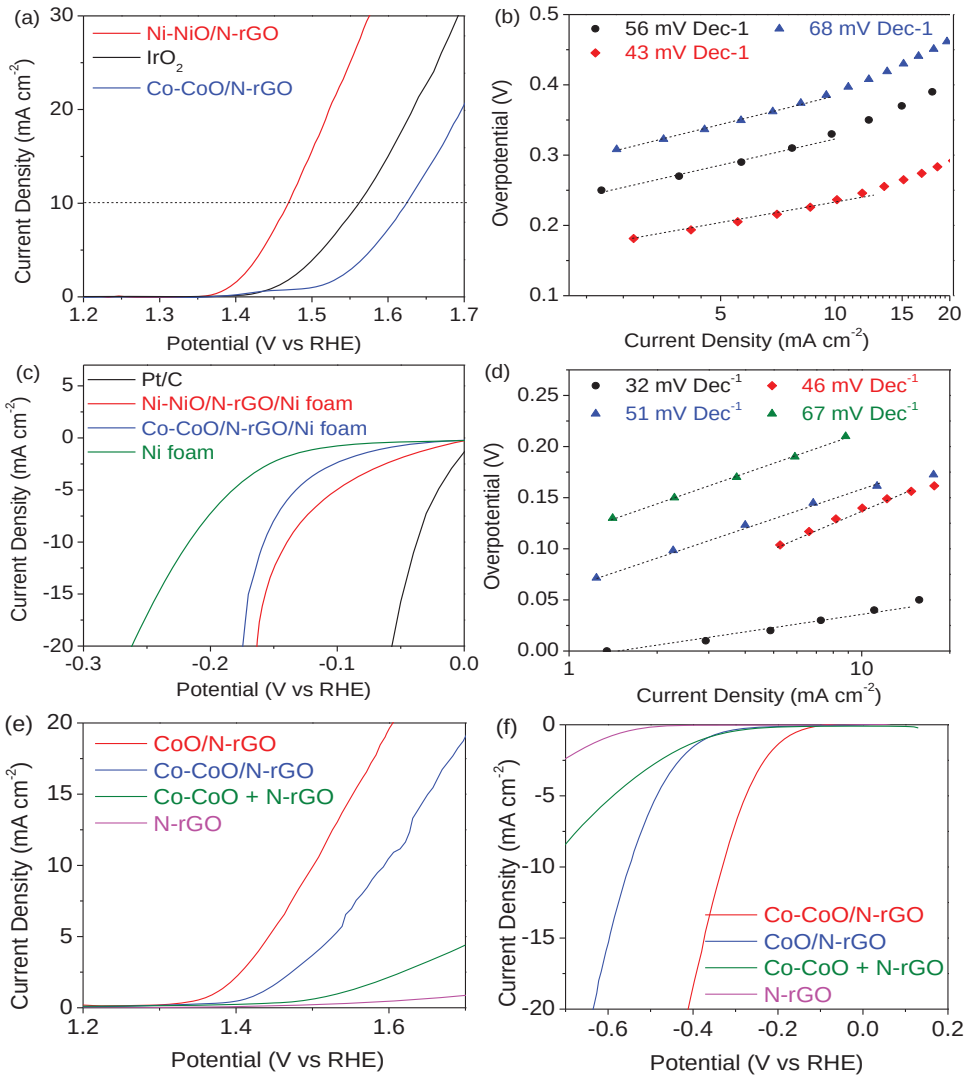

Figure 4. a) OER polarization curves of Ni-NiO/N-rGO, Co-CoO/N-rGO, and IrO_2 (glass carbon electrodes). b) OER Tafel plots obtained from the OER polarization curves. c) HER polarization curves of Ni-NiO/N-rGO, Co-CoO/N-rGO, Pt/C, and Ni foam (scanning rate is 5 mV s^{-1}, rotating rate is 1600 rpm, and the loading is 1 mg). d) HER Tafel plots obtained from the HER polarization curves. e) OER polarization curves of CoO/N-rGO, Co-CoO/N-rGO, Co-CoO+N-rGO, and N-rGO. f) HER polarization curves of CoO/N-rGO, Co-CoO/N-rGO, Co-CoO+N-rGO, and N-rGO on glass carbon electrode (scanning rate: 10 mV s^{-1}, rotating rate: 1600 rpm, and the loading is 0.21 mg cm^{-2}).

kinetic for the OER, relative to Co-CoO/N-rGO. We also compared Ni-NiO/N-rGO with other reported highly efficient OER electrocatalysts and summarized in Table S1 (Supporting Information). Notably, Ni-NiO/N-rGO is one of the most active OER catalysts in alkaline media.

Furthermore, HER polarization plots measured with Ni-NiO/N-rGO/Ni foam, Co-CoO/N-rGO/Ni foam, Pt/C and Ni foam in 1.0 M KOH are shown in Figure 4c. When a catalyst loading is around 1.0 mg cm^{-2}, the overpotentials measured at a current density of 20 mA cm^{-2} for the Ni-NiO/N-rGO/Ni foam and Co-CoO/N-rGO/Ni foam electrodes are 0.16 and 0.17 V, respectively. These values are the lowest among ever reported precious-metal-free HER catalysts in alkaline solutions as compared in Table S2 (Supporting Information). Although the used bare Ni foam support is also active for the HER with an overpotential of 0.26 V, incorporating such Ni- and Co-based graphene catalysts is able to significantly reduce the overpotentials and enhance the catalytic activity for the HER. In addition, Tafel slopes for the HER were calculated to be 46 and 51 mV dec^{-1} for Ni-NiO/N-rGO/Ni foam and Co-CoO/N-rGO/Ni foam, respectively (Figure 4d). Both are lower than reported precious-metal-free HER catalysts in alkaline solutions (Table S2, Supporting Information), indicating different rate-determined step compared to other traditional transition metal catalysts. Compared to our studied nonprecious metal catalysts, the commercial Pt/C still exhibits the smallest overpotential of 0.06 V with the highest activity for the HER. To elucidate the role of each component in these composite catalysts in promoting the OER and HER activities, CoO/N-rGO, Co-CoO+N-rGO, and N-rGO control samples (coated on glass carbon electrodes with the loading of 0.21 mg cm^{-2}) were studied in terms of their OER and HER activities by measuring their linear scan voltammograms and

compared with Co-CoO/N-rGO (Figure 4e,f). Among these cobalt-based materials, CoO/N-rGO demonstrated the highest activity for the OER, suggesting that Co^{2+} plays pivotal role for the OER. Meanwhile, the CoO/N-rGO showed much smaller charge transfer resistance (R_{ct}) (≈20 Ω) for the OER compared to that of Co-CoO/N-rGO (≈30 Ω), indicating a fast reaction rate (Figure S6a, Supporting Information). In addition, the Co-CoO+N-rGO and N-rGO exhibit much lower activities than those of CoO/N-rGO and Co-CoO/N-rGO, indicating that the intimated interaction between metal/metal oxide and graphene supports is crucial for improving the catalytic activity (Figure 4e). HER activities of Co-CoO/N-rGO, CoO/N-rGO, Co-CoO+N-rGO, and N-rGO were also evaluated and compared in Figure 4f, Co-CoO/N-rGO exhibits the highest activity, superior to the physically mixtured Co-CoO+N-rGO and standalone N-rGO. This comparison indicates that Co^0 is dominant active species for the HER and CoO is necessary for further improving the activity. Therefore, we speculate that Co^0 and Co^{2+} species may be synergistic active sites for the HER catalysis and the possible mechanism could be described by Volmer–Tafel and Volmer–Heyrovsky pathways in basic media.[35,36]

$$H_2O + e^- \rightarrow H_{ads} + OH^- \text{ (Volmer)} H_{ads} + H_{ads} \rightarrow H_2 \text{ (Tafel)} \quad (1)$$

$$H_2O + e^- \rightarrow H_{ads} + OH^- \text{ (Volmer)} H_{ads} + H_2O + e^- \rightarrow H_2 + OH^- \text{ (Heyrovsky)} \quad (2)$$

Both Volmer–Tafel and Volmer–Heyrovsky pathways involve the absorption of H_2O molecule. Subsequently, the H_2O is dissociated into adsorbed H atom and OH^-. Finally, the OH^- is detached from the surface and the adsorbed H is transformed into H_2. Previous reports indicated that metal Co has a suitable binding energy for H atom (close to Pt)[37,38] and CoO can be hydroxylated to dissociation H_2O.[39–41] Thus, as for the Co-CoO/N-rGO catalyst, the OH^- from the dissociation of H_2O is favorable on CoO surface because Co^{2+} species has strong electrostatic affinity, while nearby Co sites facilitate to H atom adsorption, yielding a synergistic effect between metal Co and CoO for the HER. As expected, due to the presence of metallic Co sites to provide H adsorption sites, CoO/N-rGO exhibited relatively low HER activity. Also, physically mixed Co-CoO+N-rGO was also not favorable for the HER due to that the synergistic effect is unlikely between weakly coupling metal/metal oxides and N-rGO. The OER and HER activities of Ni-NiO+N-rGO and β-$Ni(OH)_2$/rGO were also compared with Ni-NiO/N-rGO in Figure S4a,b (Supporting Information). While Ni-NiO+N-rGO shows much higher activity than that of β-$Ni(OH)_2$/rGO, the Ni-NiO/N-rGO demonstrated the highest activity for both OER and HER. We also studied he HER activities of Ni-NiO/N-rGO and Co-CoO/N-rGO catalysts by directly coating them on glass carbon electrodes. The measured HER activities are obviously lower than that obtained by using bare Ni foam. However, when depositing Ni-NiO/N-rGO and Co-CoO/N-rGO on Ni form, these catalysts exhibited much enhanced HER activities relative to the Ni foam itself, indicating a possible synergetic effect of Ni-NiO/N-rGO and Co-CoO/N-rGO with Ni foam (Figure S5, Supporting Information).

The ORR polarization plots for the CoO/N-rGO, Co-CoO/N-rGO, and Pt/C were measured using a rotating-disk electrode (RDE) in 0.1 M KOH (**Figure 5**a). The ORR data from Ni-NiO/N-rGO did not presented because of its poor activity. In the case of the Co-CoO/N-rGO catalyst, the measured current density slowly increased in the range from 0.95 to 0.86 V and rapidly increased to 0.73 V in the mixed kinetic-diffusion control region followed by a well-defined diffusion-limiting current density. The onset and $E_{1/2}$ potentials measured with the Co-CoO/N-rGO are ≈0.88 and 0.78 V, respectively. In the absence of metallic Co, CoO/N-rGO sample exhibited a lower activity, relative to the Co-CoO/N-rGO. Under identical experimental conditions, the onset potential and $E_{1/2}$ of Pt/C (20% Pt on Vulcan XC-72) were measured at 0.85 and 0.98 V, respectively. Although the studied Co-CoO/N-rGO is still underperforming to the state-of-the-art Pt/C catalyst, it is comparable to the ever reported highly efficient ORR oxide catalysts as compared in Table S3 (Supporting Information). It is worth noting that Co-CoO/N-rGO exhibited a similar Tafel slope (40 mV dec^{-1}) compared to that of Pt/C (38 mV dec^{-1}) in the low current density region (Figure 5b), suggesting a similar rate-determined step during the ORR. Furthermore, the polarization plots collected at different rotating speeds were used to analyze the ORR kinetics for the Co-CoO/N-rGO catalyst (Figure 5c). The corresponding Koutecky–Levich plots (j^{-1} vs $\omega^{-1/2}$) at different potentials were displayed in the inset of Figure 5c, which is typical of first-order reaction kinetics to the concentration of dissolved O_2 characterized by linearity of plots. The kinetic parameters can be analyzed by the following equations:[42]

$$\frac{1}{j} = \frac{1}{j_k} + \frac{1}{j_l} = \frac{1}{B\omega^{1/2}} + \frac{1}{j_k} \quad (3)$$

$$B = 0.2nFC_{O_2}D_{O_2}^{2/3}\upsilon^{-1/6} \quad (4)$$

$$j_k = nFkC_o \quad (5)$$

where j is the measured current density, j_k and j_l are the kinetic and diffusion-limiting current densities, respectively, and ω is the rotating rate of electrode (rpm). B is determined from the slope of the Koutecky–Levich plots according to the Levich equation. n is electron transfer number per oxygen molecule, F is Faraday constant (96 485 C mol^{-1}), C_{O2} is the bulk concentration of O_2 (7.8×10^{-7} mol cm^{-3}), and υ is the kinetic viscosity of electrolyte (0.01 cm^2 S^{-1}). D_{O2} is the diffusion coefficient of O_2 in 1 M KOH (1.8×10^{-5} cm^2 S^{-1}). The inverse current is a function of the inverse square root of the rotation speeds at varied potentials. The electron transfer number (n) was calculated from the slopes of K-L plots to be 3.7–3.9 at potentials of 0.50–0.60 V, indicating a four-electron pathway during the ORR. Hydrogen peroxide yields was also calculated by the following equations:[43]

$$\%(HO_2^-) = 200 \times \frac{\frac{I_r}{N}}{I_d + \frac{I_r}{N}} \quad (6)$$

where I_d is disk current, I_r is ring current, and the collection efficiency (N) was determined to be 0.40 by using 10×10^{-3} M $K_3[Fe(CN)_6]$. The HO_2^- yield was calculated to be ≈10% for

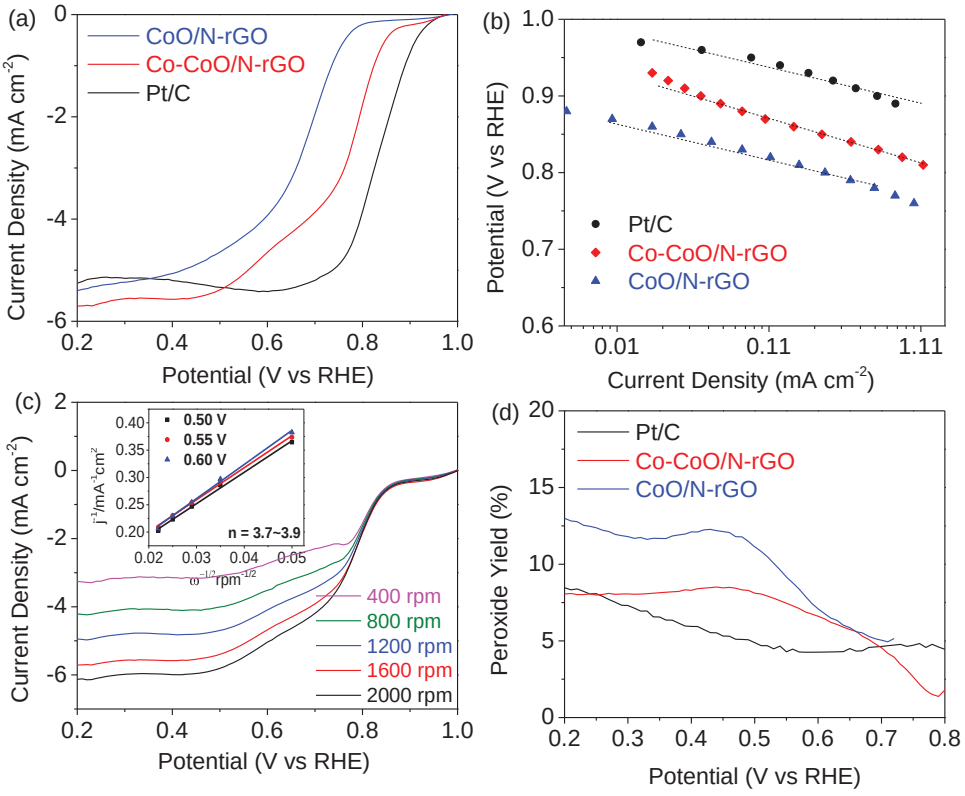

Figure 5. a) ORR polarization curves of CoO/N-rGO, Co-CoO/N-rGO, and Pt/C (scanning rate: 10 mV s^{-1}, rotating rate: 1600 rpm, and the loading is 0.21 mg cm^{-2}). b) ORR Tafel plots obtained from the ORR polarization curves. c) ORR polarization curves of Co-CoO/N-rGO at various rates and K-L plots (inset). d) Peroxide yields of Co-CoO/N-rGO and Pt/C.

the Co-CoO/N-rGO that is comparable to that of Pt/C in the region from 0.20 to 0.55 V (Figure 5d). Oppositely, the CoO/N-rGO sample generates a much higher HO_2^- yield than that of Pt/C in the same region. We also prepared N-rGO sample under identical conditions except for omitting cobalt salt. In Figure S4c (Supporting Information), compared to other ratios of Co to GO, the catalytic activities of CoO/N-rGO prepared from 100 mg GO showed the highest catalytic activities, indicating proper content of rGO in catalysts is very important to producing high activity. An increasing catalytic activity for the ORR was obtained following this order: N-GO < CoO/N-rGO < Co-CoO/N-rGO. The charge transfer resistances were simulated by fitting Nyquise plots using an equivalent circuit. The Co-CoO/N-rGO showed the smallest charge transfer resistance (R_{ct}) (≈550 Ω) for the ORR compared to that of CoO/N-rGO (≈1100 Ω). The R_{ct} can be directly correlated to the ORR reactivity (Figure S6b, Supporting Information), indicating a fast reaction kinetic on Co-CoO/N-rGO.

In order to further determine the stability of these newly developed Ni- and Co-based catalysts during the studied electrochemical reactions. At first, chronopotentiometric measurement of Ni-NiO/N-rGO for the OER was conducted at a constant potential of 1.50 V versus time (extending to 40 000 s) in 0.1 M KOH (**Figure 6**a, top). A slight increase in the current density is observed within 10 000 s. Subsequently, a current density of ≈16 mA cm^{-2} is remained up to 40 000 s. For the HER stability of Ni-NiO/N-rGO/Ni foam (Figure 6a, bottom), an initial current density of ≈–10 mA cm^{-2} generated at a constant potential of –0.15 V versus reversible hydrogen electrode (RHE) in 1 M KOH is slightly decreased during the long-term stability test. To further determine the stability of Co-CoO/N-rGO under the HER and ORR operation models, we investigated the generated current densities as a function of time under continuous constant operation potentials up to 20 000 s. Stable current densities of around –2.0 (Figure 6b, top) and –10 mA cm^{-2} (Figure 6b, bottom) were maintained at constant potentials of 0.75 V for the ORR in 0.1 M KOH and – 0.15 V for the HER in 1.0 M KOH, respectively.

Because the Co-CoO/N-rGO exhibited good ORR activity, we further evaluated the performance of zinc-air batteries using Co-CoO/N-rGO-based air cathodes. An optical photography of zinc-air battery we designed for this experiment was shown in Figure S7 (Supporting Information). The galvanostatic discharge curves of zinc-air batteries were tested at a current density of 35 mA cm^{-2} in a 6.0 M KOH electrolyte under ambient air (**Figure 7**a). The Co-CoO/N-rGO is able to maintain an average voltage plateau (1.08 V) that is comparable to Pt/C-based battery. A slightly potential drop was observed for each sample after a galvanostatic discharge up to 2 h, indicating a good catalytic stability for the ORR in 6.0 M KOH. Figure 7b shows the cathodic and anodic polarization curves of Co-CoO/N-rGO- and ($Pt/C+IrO_2$)-based Zn-air batteries. The Co-CoO/N-rGO-based battery showed a sum of polarization charging and discharging overpotentials (ΔV = 1.26 V) at a current density of 50 mA cm^{-2},

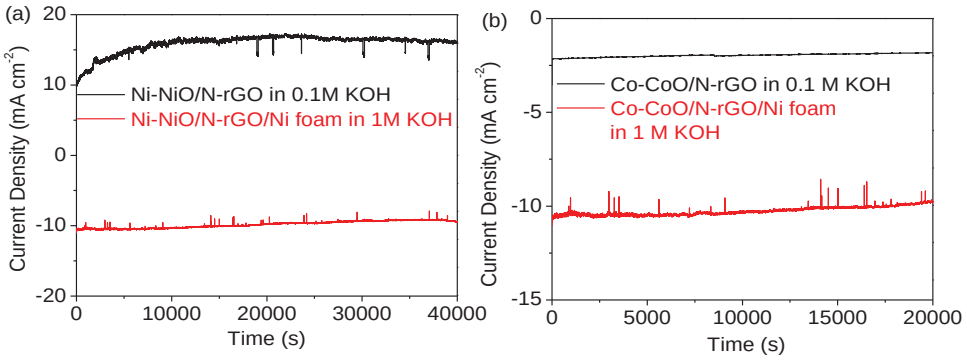

Figure 6. a) Chronopotentiometry (*j*–*t*) measurements of Ni-NiO/N-rGO for OER (top) and HER (bottom) at the constant potentials of 1.50 and –0.15 V (vs RHE) in 0.1 and 1 M KOH, respectively. b) Chronopotentiometry (*j*–*t*) measurements of Co-CoO/N-rGO for ORR (top) and HER (bottom) at the constant potentials of 0.7 and –0.15 V (vs RHE) in 0.1 and 1 M KOH, respectively.

which is comparable to the (Pt/C+IrO_2)-based battery (ΔV = 1.22 V). The individual Co-CoO/N-rGO catalyst exhibited lower activity compared to Pt/C in the RDE tests, however, in real zinc-air battery tests, Co-CoO/N-rGO has improved performance approaching to Pt/C+IrO_2 cathode. The major reason is due to the graphene in the composite catalyst, providing enhanced electrical conductivity and high surface area for the Co-based catalysts. Generally, graphene can help to improve the interaction between catalysts and gas diffusion layer with minimized electrical contact resistance. In addition, the discrepancy of activity measured from traditional rotating disk electrode (RDE) and real metal-air battery could be due to the different testing conditions. At first, the concentrations of KOH for RDE and battery tests are different. We measured the ORR using RDE with 0.1 M KOH and tested the zinc-air batteries in 6 M KOH. We used 6 M KOH in zinc-air batteries because a high concentration of KOH is favorable to electrical conductivity in a practical device (zinc-air batteries). The structure of air cathode is more complicated. The porous air cathodes were fabricated by coating the catalysts on the gas diffusion layer that was prepared by heating a mixture of the activated charcoal and polytetrafluoroethylene (PTFE) on a nickel mesh. Thus, although the Co-CoO/N-rGO catalyst exhibited inferior activity in RDE test to Pt/C, lower electrical resistance, and favorable mass transfer due to porous graphene cathode layers lead to improved performance for the Co-based catalyst in zinc-air batteries. Thus, the Co-CoO/N-rGO catalyst is able to demonstrate comparable performance to Pt/C+IrO_2 cathode, holding promise to replace precious-metal-based catalysts for rechargeable zinc-air batteries.

3. Conclusions

We reported a new class of composite electrocatalysts by integrating metallic (Ni or Co) with their oxides (NiO or CoO), further dispersed onto nitrogen-doped rGO, i.e., Ni-NiO/N-rGO and Co-CoO/N-rGO. Overall, both catalysts demonstrated multiple function to catalyze the OER, HER, or ORR in alkaline media. In particular, both of them showed excellent HER activity when these catalysts were coated on the Ni foam electrodes. Ni-NiO/N-rGO outperformed most of reported precious-metal free catalysts for the OER. Meanwhile, the Co-CoO/N-rGO exhibited the higher ORR activity, relative to Ni-based catalysts. Its ORR activity was further studied as air cathode in a primary zinc-air battery, achieving comparable performance to the Pt/C cathode. Importantly, the charging and discharging polarization tests of Co-CoO/N-rGO indicated that the nonprecious metal cathode is able to approach the performance of Pt/C+IrO_2 cathode in rechareable zinc-air batteries. The work may open a new

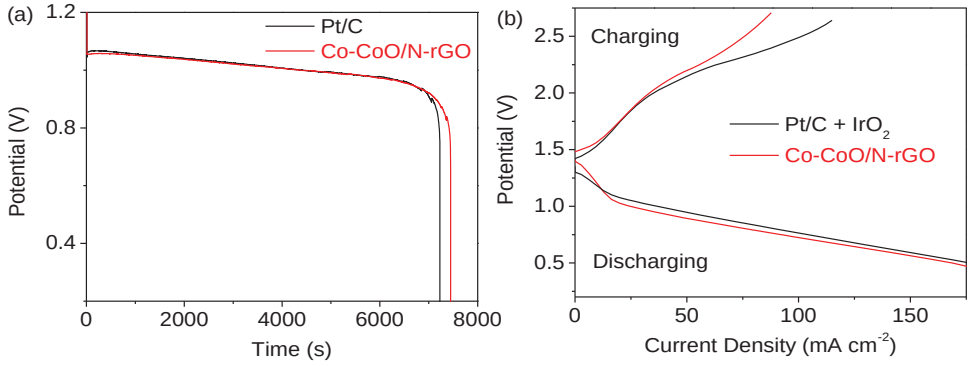

Figure 7. a) Duration measurement under constant discharge current density (35 mA cm^{-2}) using the Co-CoO/N-rGO- and Pt/C-based air cathodes. b) Charge and discharge polarization curves of two-electrode zinc-air full-cell batteries of the Co-CoO/N-rGO- and (Pt/C + IrO_2)-based air cathodes in 6.0 M KOH.

avenue to prepare precious-metal-free multifunctional catalysts to replace noble-metals-based catalysts for clean electrochemical energy storage and conversion technologies.

4. Experimental Section

Reagents and Chemicals: All chemicals were purchased from Sigma-Aldrich and used without further purification.

Synthesis: Graphene oxide (GO) was prepared from graphite powder (Sigma, 325 mesh) following a reported procedure.[44] $Co(CO_3)_{0.5}(OH)\cdot 0.11H_2O$-rGO was synthesized using a simple hydrothermal route.[45] CoO/N-rGO was prepared by following a reported procedure.[19] Typically, GO (0.1 g) was first dispersed in 30 mL deionized water in a glass vial. Then $Co(NO_3)_2\cdot 6H_2O$ or $Ni(NO_3)_2\cdot 6H_2O$ (2 mmol, 582 mg), urea (10 mmol, 600 mg), and NH_4F (5 mmol, 185 mg) were dissolved in 10 mL deionized water in another vial. After sonicating them for 20 min, both solutions were transferred into a 50 mL Teflon-lined stainless steel autoclave reactor that was subsequently heated at 120 °C for 12 h. Next, the resulting dark solution was filtered, sonicated, and centrifuged at 4000 rpm for 5 min. The collected dark solid $Co(CO_3)_{0.5}(OH)\cdot 0.11H_2O$-rGO or rGO/$\beta$-$Ni(OH)_2$ was dispersed in deionized water for lyophilization. Finally, CoO/N-rGO was obtained from the lyophilized $Co(CO_3)_{0.5}(OH)\cdot 0.11H_2O$-rGO in a tube furnace at 500 °C for 2 h under Ar, followed by another annealing procedure at 200 °C for 1 h under NH_3 and Ar. Meanwhile, Ni-NiO/N-rGO was obtained by the annealing of rGO/β-$Ni(OH)_2$ under the same conditions. Ni-NiO and Co-CoO were prepared using same methods but without adding graphene oxides in starting materials.

Instrumentation: XPS was measured using an Escalab instrument (Escalab 250 xi, Thermo Scientific, England) with a base pressure of 5×10^{-9} Torr using monochromatic Al Kα radiation (1486.6 eV). XRD (D/Max2000, Rigaku) was carried out by using Cu Kα radiation. The scanning electron microscope (S-4800, Hitachi) was operated at 10 kV, and HRTEM (JEOL JEM-2100F) was conducted at 200 kV. Co K-edge X-ray absorption spectra, X-ray absorption near edge structure (XANES) spectra, and extended EXAFS spectra were tested on the BL10C beam line using the Pohang Light Source (PLS-II) in Korea with top-up mode operation under a ring current of 200 mA at 3.0 G eV.

Electrochemical Measurements: The OER and ORR activities of catalysts were measured using a standard three-electrode electrochemical cell filled with a 0.1 M KOH electrolytes. A glassy carbon (4 mm diameter) coated with catalyst is the working electrode. A graphite rod and HgO/Hg electrode were used for the counter and the reference electrodes, respectively. The electrochemical impedance spectroscopy measurements were carried out using a CHI 660A electrochemical workstation under the OER and ORR operation conditions. The spectra were collected in a frequency range of 10^4–0.01 Hz with an amplitude of 5 mV. The Hg/HgO reference electrode was calibrated relative to RHE by bubbling high-purity hydrogen in KOH solution using a Pt-black electrode. The potentials were *i*R-corrected for the OER measurements determined by using high-frequency AC impedance (typically ≈50 Ω). For the ORR measurements, high-purity O_2 gas was bubbled into the solution ≈20 min before the electrochemical measurements and throughout the whole testing process. The catalysts (3.0 mg) and 60 µL of a 5 wt% Nafion solution were dispersed in 0.35 mL of ethanol and 0.15 mL of deionized water. The resulting mixture was sonicated to form a homogeneous ink. A catalyst loading of 0.21 mg cm^{-2} was applied on the surface of the glassy carbon electrode by the drop addition of 5 µL of catalyst ink. The Pt loading for the 20% Pt/Vulcan XC-72 reference catalyst was 64 μg_{pt} cm^{-2}. IrO_2 (≈5 µm, Sigma-Aldrich 99.9%) also was used as a reference. IrO_2 ink was also prepared by dispersing IrO_2 (3 mg) in a mixture of 0.35 mL of ethanol, 0.15 mL of deionized water, and 60 µL of a 5 wt% Nafion solution.

Fabrication and Measurement of Zinc-Air Batteries: The air cathodes were prepared by coating a mixture of the activated charcoal and PTFE (the weight ratio = 7:3) on a nickel mesh to prepare a gas diffusion layer. The thickness of each air cathode was fixed to be ≈500 µm by a pressing machine. Then the catalysts (3.0 mg) and 60 µL of a 5 wt% Nafion solution were dispersed in 0.35 mL of ethanol and 0.15 mL of deionized water to prepare a homogeneous cathode ink. The 250 µL ink was carefully pasted onto the above gas diffusion layer and kept it in a vacuum oven for 30 min, followed by a mildly pressing procedure. The prepared air cathodes with a catalyst loading of 0.53 mg cm^{-2} were used to assemble zinc-air batteries. A zinc plate was used as the anode and was separated by a nylon polymer membrane with the air cathode. 6.0 M KOH solution was filled between the cathode and anode. Ni meshes were used as current collectors.

Supporting Information

Supporting Information is available from the Wiley Online Library or from the author.

Acknowledgements

This work was supported by the next generation secondary battery R&D program of MKE/KEIT (10042575). G.W. is also grateful the financial support from the startup fund of University at Buffalo, SUNY along with U.S. Department of Energy, Fuel Cell Technologies Office (FCTO) Incubator Program (DE-EE0006960).

Received: May 31, 2015
Revised: July 20, 2015
Published online: August 13, 2015

[1] A. J. Bard, M. A. Fox, *Acc. Chem. Res.* **1995**, *28*, 141.
[2] M. Lefevre, E. Proietti, F. Jaouen, J. P. Dodelet, *Science* **2009**, *324*, 71.
[3] N. Armaroli, V. Balzani, *Angew. Chem. Int. Ed.* **2007**, *46*, 52.
[4] K. S. Joya, Y. F. Joya, K. Ocakoglu, R. van de Krol, *Angew. Chem. Int. Ed.* **2013**, *52*, 10426.
[5] C. Liu, F. Li, L. P. Ma, H. M. Cheng, *Adv. Mater.* **2010**, *22*, E28.
[6] G. Wu, K. L. More, C. M. Johnston, P. Zelenay, *Science* **2011**, *332*, 443.
[7] G. Wu, P. Zelenay, *Acc. Chem. Res.* **2013**, *46*, 1878.
[8] D. Sun, Y. Shen, W. Zhang, L. Yu, Z. Q. Yi, W. Yin, D. Wang, Y. H. Huang, J. Wang, D. L. Wang, J. B. Goodenough, *J. Am. Chem. Soc.* **2014**, *136*, 8941.
[9] Y. G. Li, M. Gong, Y. Y. Liang, J. Feng, J. E. Kim, H. L. Wang, G. S. Hong, B. Zhang, H. J. Dai, *Nat. Commun.* **2013**, *4*.
[10] C.-F. Chen, G. King, R. M. Dickerson, P. A. Papin, S. Gupta, W. R. Kellogg, G. Wu, *Nano Energy* **2015**, *13*, 423.
[11] Q. Li, R. Cao, J. Cho, G. Wu, *Phys. Chem. Chem. Phys.* **2014**, *16*, 13568.
[12] Q. Li, R. Cao, J. Cho, G. Wu, *Adv. Energy Mater.* **2014**, *4*, 1301415.
[13] K. Fominykh, J. M. Feckl, J. Sicklinger, M. Doblinger, S. Bocklein, J. Ziegler, L. Peter, J. Rathousky, E. W. Scheidt, T. Bein, D. Fattakhova-Rohlfing, *Adv. Funct. Mater.* **2014**, *24*, 3123.
[14] D. Wang, G. Ghirlanda, J. P. Allen, *J. Am. Chem. Soc.* **2014**, *136*, 10198.
[15] L. Trotochaud, J. K. Ranney, K. N. Williams, S. W. Boettcher, *J. Am. Chem. Soc.* **2012**, *134*, 17253.
[16] S. J. Guo, S. Zhang, L. H. Wu, S. H. Sun, *Angew. Chem. Int. Ed.* **2012**, *51*, 11770.
[17] P. Quaino, F. Juarez, E. Santos, W. Schmickler, *Beilstein J. Nanotechnol.* **2014**, *5*, 846.

[18] Q. Li, P. Xu, B. Zhang, H. Tsai, J. Wang, H.-L. Wang, G. Wu, *Chem. Commun.* **2013**, *49*, 10838.
[19] Q. G. He, Q. Li, S. Khene, X. M. Ren, F. E. Lopez-Suarez, D. Lozano-Castello, A. Bueno-Lopez, G. Wu, *J. Phys. Chem. C* **2013**, *117*, 8697.
[20] G. Wu, H. T. Chung, M. Nelson, K. Artyushkova, K. L. More, C. M. Johnston, P. Zelenay, *ECS Trans.* **2011**, *41*, 1709.
[21] S. J. Guo, S. H. Sun, *J. Am. Chem. Soc.* **2012**, *134*, 2492.
[22] Q. Li, P. Xu, W. Gao, S. Ma, G. Zhang, R. Cao, J. Cho, H.-L. Wang, G. Wu, *Adv. Mater.* **2014**, *26*, 1378.
[23] G. Wu, N. H. Mack, W. Gao, S. Ma, R. Zhong, J. Han, J. K. Baldwin, P. Zelenay, *ACS Nano* **2012**, *6*, 9764.
[24] Y. Y. Liang, Y. G. Li, H. L. Wang, J. G. Zhou, J. Wang, T. Regier, H. J. Dai, *Nat. Mater.* **2011**, *10*, 780.
[25] S. Chen, J. J. Duan, J. R. Ran, M. Jaroniec, S. Z. Qiao, *Energy Environ. Sci.* **2013**, *6*, 3693.
[26] G. F. Cai, J. P. Tu, J. Zhang, Y. J. Mai, Y. Lu, C. D. Gu, X. L. Wang, *Nanoscale* **2012**, *4*, 5724.
[27] L. H. Zhuo, J. C. Ge, L. H. Cao, B. Tang, *Cryst. Growth Des.* **2009**, *9*, 1.
[28] K. M. Nam, J. H. Shim, D. W. Han, H. S. Kwon, Y. M. Kang, Y. Li, H. Song, W. S. Seo, J. T. Park, *Chem. Mater.* **2010**, *22*, 4446.
[29] X. Guan, J. W. Nai, Y. P. Zhang, P. X. Wang, J. Yang, L. R. Zheng, J. Zhang, L. Guo, *Chem. Mater.* **2014**, *26*, 5958.
[30] C. L. Gao, Y. Y. Liang, M. Han, Z. Xu, J. M. Zhu, *J. Phys. Chem. C* **2008**, *112*, 9272.
[31] M. H. Yu, W. Wang, C. Li, T. Zhai, X. H. Lu, Y. X. Tong, *NPG Asia Mater.* **2014**, *6*.
[32] A. Y. Khodakov, A. Griboval-Constant, R. Bechara, F. Villain, *J. Phys. Chem. B* **2001**, *105*, 9805.
[33] A. N. Mansour, C. A. Melendres, *J. Phys. Chem. A* **1998**, *102*, 65.
[34] L. Sciortino, F. Giannici, A. Martorana, A. M. Ruggirello, V. T. Liveri, G. Portale, M. P. Casaletto, A. Longo, *J. Phys. Chem. C* **2011**, *115*, 6360.
[35] M. Gong, W. Zhou, M. C. Tsai, J. Zhou, M. Guan, M. C. Lin, B. Zhang, Y. Hu, D. Y. Wang, J. Yang, S. J. Pennycook, B. J. Hwang, H. Dai, *Nat. Commun.* **2014**, *5*, 4695.
[36] G. Wu, N. Li, C. S. Dai, D. R. Zhou, *Mater. Chem. Phys.* **2004**, *83*, 307.
[37] C. Lupi, A. Dell'Era, M. Pasquali, *Int. J. Hydrogen Energy* **2009**, *34*, 2101.
[38] W. C. Sheng, M. Myint, J. G. G. Chen, Y. S. Yan, *Energy Environ. Sci.* **2013**, *6*, 1509.
[39] H. Y. Jin, J. Wang, D. F. Su, Z. Z. Wei, Z. F. Pang, Y. Wang, *J. Am. Chem. Soc.* **2015**, *137*, 2688.
[40] S. C. Petitto, E. M. Marsh, G. A. Carson, M. A. Langell, *J. Mol. Catal., A* **2008**, *281*, 49.
[41] X. L. Xu, J. Q. Li, *Surf. Sci.* **2011**, *605*, 1962.
[42] G. Wu, G. Cui, D. Li, P.-K. Shen, N. Li, *J. Mater. Chem.* **2009**, *19*, 6581.
[43] G. Wu, C. M. Johnston, N. H. Mack, K. Artyushkova, M. Ferrandon, M. Nelson, J. S. Lezama-Pacheco, S. D. Conradson, K. L. More, D. J. Myers, *J. Mater. Chem.* **2011**, *21*, 11392.
[44] Y. Zheng, Y. Jiao, L. Ge, M. Jaroniec, S. Z. Qiao, *Angew. Chem. Int. Ed.* **2013**, *52*, 3110.
[45] Q. Guan, J. L. Cheng, B. Wang, W. Ni, G. F. Gu, X. D. Li, L. Huang, G. C. Yang, F. D. Nie, *ACS Appl. Mater. Interfaces* **2014**, *6*, 7626.